nature communications

Article

https://doi.org/10.1038/s41467-025-63668-9

Phase-selective synthesis and polymorphic transformation of crystalline red phosphorus

Received: 14 February 2025

Accepted: 19 August 2025

Published online: 29 September 2025

Check for updates

Wujia Chen, Bowen Zhang, Qiang Li & Qingfeng Yan

Recent advances in black phosphorus have renewed interest in elemental phosphorus, sparking a resurgence in the study of its allotropes, especially crystalline red phosphorus (RP). Although progress has been made in synthesizing various crystalline RP phases, current strategies often rely on specific precursor formulations, limiting their scalability for industrial applications. A unified gas-phase method enabling phase-selective synthesis under consistent conditions remains elusive, and the underlying mechanisms governing polymorphic transformations are not yet fully understood. Herein, we achieve the phase-selective synthesis of crystalline RP powders via a solid-phase thermal transformation (STT) method. Extensive experiments were conducted to elucidate the synthetic mechanism of the STT method. The gas-phase molecule-mediated (GPM) solid-solid phase transition model was proposed to describe the synthesis process. Additionally, we demonstrated the sequential transition of Form II-Form IV-Form V RP from both thermodynamic and kinetic perspectives, and clarified the specific structural evolution pathways through first-principles calculations. A theoretical framework based on Ostwald's rule was developed, integrating temperature- and time-controlled methods to guide the polymorphic transformation of crystalline RP. Our work advances the understanding of selective synthesis and phase transitions of phosphorus, laying the foundation for the study of polymorphic transformations in non-metal elements.

Over the past decade, black phosphorus, as a rediscovered two-dimensional elemental semiconductor, has attracted increasing attention due to significant advances in gas-phase synthesis[1–4] and formation mechanism studies[5] as well as its great potential in semiconductor applications[6–8]. This resurgence has not only reawakened interest in this ancient and mysterious non-metal element, but also catalyzed a renaissance in the study of its allotropes. Red phosphorus (RP), a representative allotrope of elemental phosphorus, has undergone significant advancements in its classification and structural characterization in the past century, marking a remarkable journey, despite twists and turns. In 1947, Roth et al. classified RP into five modifications based on the conversion temperature, designating them as Form I to Form V RP (hereafter referred to as Form I to V)[9], where Form I is amorphous and the others are crystalline. Among the known forms, only Form II, IV, and V can be reliably reproduced experimentally, while Form III was only mentioned in the early work and has not been reported thereafter[9]. In 1969, after a series of studies spanning 15 years, the Krebs group determined the structure of Form V to be monoclinic through single-crystal analysis[10–12]. The structure of Form IV was fully resolved by Rcuk in 2005, following the synthesis of high-quality single crystals by gas-phase methods[13]. Even in the complex structural analysis of Form II, breakthrough progress has recently been

Engineering Research Center of Advanced Rare Earth Materials, Ministry of Education, Department of Chemistry, Tsinghua University, Beijing, PR China.
e-mail: yanqf@mail.tsinghua.edu.cn

achieved, leading to the successful determination of its unit cell parameters and possible structural models[14,15]. These advances in structural determination have laid the foundation for understanding the intrinsic structural motifs and their implications. The three known crystalline forms of RP exhibit distinct structural features: wavy packing of twisted phosphorus tubes (Form II), quasi-one-dimensional phosphorus tubes (Form IV), and two-dimensional stacking (Form V). The unique physical properties associated with these architectures make them suitable for a range of potential applications, such as catalysis[16], flame retardancy[17], semiconductor devices[18], and linear/nonlinear optical components[19,20].

Accordingly, reliable and controllable synthetic methods are essential prerequisites for further exploration of the physical properties and potential applications of crystalline RP. In recent years, significant efforts have been devoted to developing synthetic strategies for accessing high-quality crystalline RP. Among the known crystalline forms, reports on the synthesis of Form II are relatively scarce. In 2009, Winchester and colleagues synthesized single-crystalline nanorods of Form II from white phosphorus by thermal annealing under an inert atmosphere, marking an important turning point in recent research on Form II RP[21]. For Form IV, following Ruck's synthesis of bulk Form IV via chemical vapor transport (CVT) for single-crystal structure determination, Nilges and co-workers subsequently synthesized millimeter-sized single crystals of pure-phase Form IV through a short-way transport reaction using $CuCl_2$ as a mineralizer, achieving the largest crystal size reported to date[22]. In addition to bulk crystals, Form IV has also been synthesized in the form of nanowires[23], nanorods[24], flakes[25], and micropillar arrays[26] by tuning precursor compositions and temperature parameters. A similar strategy applies to Form V: millimeter-sized bulk single crystals can be obtained from an aRP/SnI_4/Sn system at 650 °C[27], while switching the reaction system to aRP/I_2/Bi enables the direct growth of Form V flakes on substrates at 550 °C[28]. After over a decade of development, the gas-phase synthesis of crystalline RP has become increasingly mature. Established protocols now allow for the selective preparation of Form II, IV, and V with tunable morphologies and sizes through specific precursor or temperature formulations. Although this strategy has proven effective for laboratory-scale synthesis, significant challenges arise when the synthesis of crystalline RP needs to be extended to practical or industrial production. In practical production, substantial variations in precursor composition and reaction conditions hinder equipment adaptability and safety, requiring phase-specific evaluation and design for each crystalline form of RP. Therefore, developing a simple gas-phase synthesis method that enables the selective formation of various crystalline phases of RP by varying reaction time under uniform feedstock and temperature conditions is particularly important, as it represents a critical step toward bridging laboratory-scale synthesis and practical industrial applications. In addition to synthesis, another critical issue lies in understanding the polymorphic transformation mechanisms of various crystalline phases of RP. Previous studies have extensively examined both the mechanisms of conventional CVT reactions[29] and the gas-phase formation pathways of specific phosphorus allotropes through quantum chemical approaches[5,25]. However, most of these investigations have focused on the transformation between amorphous and a specific crystalline phase of RP. In contrast, whether polymorphic transformation exists among the three known crystalline forms of RP—Form II, Form IV, and Form V—and the mechanisms that govern such transitions remain largely unexplored. In-depth investigation and understanding of the polymorphic transformations among different crystalline forms of RP are indispensable for constructing a unified theoretical framework for elemental phosphorus phase transitions.

Herein, we achieved the phase-selective synthesis of crystalline RP powders via a solid-phase thermal transformation (STT) method based on a low-temperature CVT reaction system, accompanied by a systematic characterization of the crystalline products. We proposed the gas-phase molecule-mediated (GPM) solid-solid phase transition model to explain the synthesis process. The synthetic mechanism of the STT was investigated further, which is attributed to the iodine-catalyzed sublimation effect, transport rate control and continuous evolution of crystalline RP. Additionally, we identified the phase transition sequence and rate of crystalline RP from both thermodynamic and kinetic perspectives, revealing the structural evolution process of Form II-Form IV-Form V through first-principles calculations. Finally, a theoretical framework grounded in the Ostwald's rule was proposed to guide the synthesis and polymorphic transformation of crystalline RP.

Results

Synthesis and growth mechanism of three high-quality crystalline RP powders

Form II, Form IV, and Form V crystalline RP powders were synthesized through a STT method based on a low-temperature CVT reaction system. In detail, commercial amorphous RP (aRP) and iodine were placed in the hot end of a quartz ampule with a neck and sand core, as schematically illustrated in Fig. 1a. Upon controlled thermal treatment, three representative crystalline RP powders are on-site formed at the hot end via continuous thermal transformation under different holding times, whereas polycrystalline RP films emerge at the cold end as secondary byproducts (Supplementary Figs. 1–5). Figure 1b illustrates the preset temperature parameters at the hot end, where a stable 15 °C temperature gradient is maintained throughout the reaction. Unlike conventional CVT methods that require high temperatures (> 550 °C) and complex multi-stage temperature control, the STT method enables the synthesis of crystalline RP through a simple low-temperature (465 °C) three-step process: heating, maintaining constant temperature, and cooling. Moreover, by controlling the holding time during the constant temperature stage, Form II, Form IV, and Form V crystalline RP can be selectively obtained at the hot end after 0.5 h, 4 h, and 30 h, with corresponding yields of 98.8%, 89.1%, and 15.0%, respectively, based on the initial 400 mg of aRP feedstock (Supplementary Fig. 6). Figure 1c shows scanning electron microscopy (SEM) images of the precursor and obtained crystalline RP: aRP precursor appears as irregular bulk particles, Form II as nanostructured rods, and Forms IV and V with distinctive one-dimensional (1D) fibrous and two-dimensional (2D) flake-like morphologies. Besides, the aRP appears purplish-red, with Form II and Form IV progressively lighter shades of deep red, and Form V the lightest in orange-red (Fig. 1c, inset). These color differences facilitate easy differentiation between the crystalline forms of RP. Powder X-ray diffraction (PXRD) and Raman spectra were performed to verify the phase structure and purity of the samples. As shown in Fig. 1d, all three crystalline RP present sharp characteristic diffraction peaks consistent with those of the standard cards, which demonstrates the high crystallinity and phase purity. Figure 1e depicts the typical Raman vibration modes of the crystalline RP. Form IV and V, with low symmetry, exhibit similar and complex Raman vibration modes due to their shared structural units [P8]P2[P9]P2. The key difference, stemming from their parallel/vertical arrangement, is the characteristic peak at 490 cm^{-1} in Form V, often used for easy identification[30]. In contrast, Form II, with even lower symmetry, displays a broader, more diffuse peak between 370 and 470 cm^{-1}, serving as its experimental signature[15]. Moreover, high-resolution X-ray photoelectron spectroscopy (XPS) shows that the binding energy of P-P bonds is around 130 eV. By fitting, the two peaks can be divided into P $2p_{1/2}$ (130.70 eV) and P $2p_{3/2}$ (129.85 eV), confirming that elemental phosphorus maintains a single valence state across the three crystalline RP (Fig. 1f and Supplementary Figs. 7–9). The minor broad peak at 134 eV is attributed to the inevitable slight oxidation during testing. Meanwhile, optical characteristics of the three crystalline RP were investigated. The ultraviolet-visible-near infrared (UV-vis-NIR) absorption spectra and the corresponding Tauc-plot curves demonstrate the light-harvesting capability of crystalline

https://doi.org/10.1038/s41467-025-63668-9

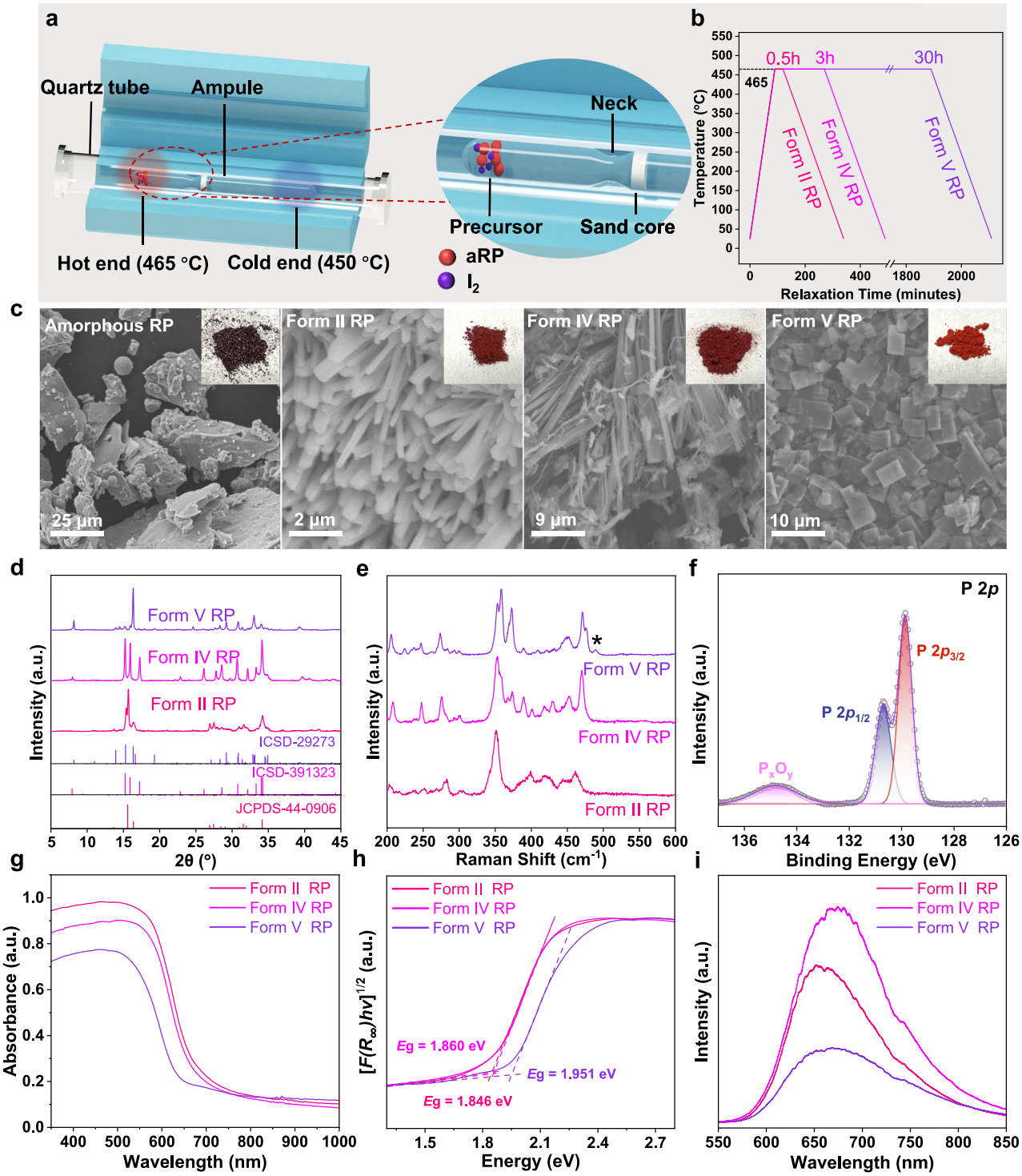

Fig. 1 | Synthesis and characterization of three crystalline red phosphorus (RP) powders. a Schematic diagram of the solid-phase thermal transformation (STT) synthesis setup based on a CVT reaction system. **b** Temperature profiles of the hot end during the reaction process. **c** Scanning electron microscopy (SEM) images of the different forms of RP. Inset: Images of different RP powders. **d** Powder X-ray diffraction (PXRD) patterns of Form II, IV, and V compared with standard reference patterns. The unit of intensity is arbitrary units (a.u.). **e** Raman spectrum of Form II, IV, and V, measured under 532 nm excitation. The "*" marks the Raman vibration peak at 490 cm^{-1}, used to distinguish between Form IV and V. **f** High-resolution X-ray photoelectron spectroscopy (XPS) of P 2*p* in Form II. **g** Ultraviolet-visible-near infrared (UV-vis-NIR) absorption spectra **h** and corresponding Tauc-plot curves of Form II, IV, and V. Note: Since the three crystalline RP are indirect bandgap semiconductors, n is 1/2 in the $[F(R_\infty)h\nu]^n = A(h\nu - E_g)$ according to previous report[50]. **i** Photoluminescence (PL) spectra of Form II, IV, and V.

RP in the visible region, revealing optical bandgaps for Form II (1.846 eV), Form IV (1.860 eV) and Form V (1.965 eV), consistent with the observed color variations (Fig. 1g, h). Figure 1i displays the photoluminescence (PL) spectrum of the crystalline RP, where the broadening of the emission peak is due to strong phonon scattering at room temperature[31]. Through fitting, the PL emission peaks of all three crystalline RP forms are centered around 674 nm, with significant differences in peak intensity: Form IV exhibits the strongest PL emission, followed by Form II, while Form V shows the weakest emission (Supplementary Fig. 10 and Fig. 1i).

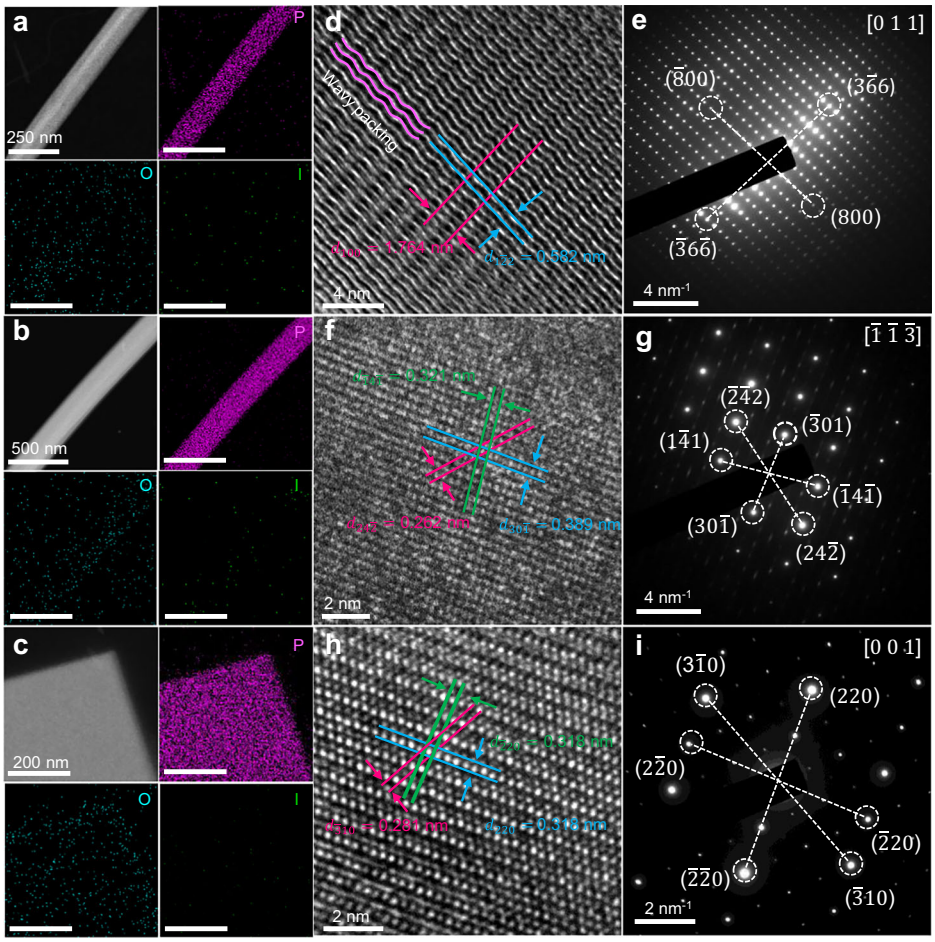

Fig. 2 | Crystal structure characterization of the three crystalline RP. a–c Low-magnification high-angle annular dark field-scanning transmission electron microscopy (HAADF-STEM) images of Form II, IV, and V obtained via liquid exfoliation, along with the elemental mappings for P, O, and I. The scale bars in the elemental mappings are consistent with those in the HADDF images. **d**, **f**, **h** High-resolution transmission electron microscopy (HRTEM) images and (**e**, **g**, **i**) corresponding selected area electron diffraction (SAED) patterns of Form II, IV, and V, respectively. The pink wavy line denotes the "wavy packing" in the lattice fringes of Form II. The zone axis directions for the SAED patterns of Form II, IV, and V are [011], [$\bar{1}\bar{1}3$], and [001], respectively.

Supplementary Tables 1 and 2 summarize the reported morphologies and synthesis parameters of Form II, Form IV, and Form V RP obtained via vapor-phase methods. Compared with these existing methods, the STT strategy provides a unified and straightforward synthesis approach applicable to all three crystalline RP phases. It offers distinct advantages in terms of lower reaction temperature and shorter synthesis duration, thereby improving both safety and efficiency. Furthermore, the STT method yields micron-sized crystalline RP powders that can be directly applied without the need for high-energy pulverization processes required for bulk crystals, thus presenting clear advantages for potential industrial applications in areas such as catalysis and flame retardancy.

The crystal structure and crystallinity characteristics of the three crystalline RP were further analyzed using transmission electron microscopy (TEM). High-angle annular dark-field images display the inherent 1D high-aspect-ratio nanoribbon morphology of Form II and IV RP, as well as 2D rectangular nanosheets of Form V, which both exhibit continuous, uniform surfaces and well-defined straight edges, indicative of high crystal quality (Fig. 2a–c). Additionally, energy-dispersive X-ray spectroscopy (EDS) mapping confirms that the samples consist solely of phosphorus, ruling out the possibility of iodine doping, while the detected trace oxygen is attributed to minor surface oxidation. The high-resolution TEM (HRTEM) images display rare wave-stacked lattice fringes and large periodic spacing along the wave direction, which are attributed to the complex crystal structure of Form II, consistent with previous reports[14,15](Fig. 2d). The interplanar spacings parallel and perpendicular to the wave stacking direction are 0.582 nm and 1.764 nm, corresponding to the ($1\bar{2}2$) and (100) planes of Form II, respectively. As shown in Fig. 2e, the selected area electron diffraction (SAED) pattern aligns closely with the simulated electron diffraction pattern along the [011] zone axis (Supplementary Fig. 11a and 12a), displaying bright and distinct diffraction spots, indicative of the exceptionally high crystallinity of Form II. Similarly, for Form IV and Form V, the interplanar spacings correspond to their respective crystal planes (Fig. 2f–i), with SAED patterns matching the simulated patterns and showing high-quality diffraction spots (Supplementary Figs. 11b, c and 12b, c).

The STT method simplifies the temperature programming, enabling phase-selective synthesis of crystalline RP powders at reduced temperatures and significantly lowering safety risks. To enhance the instructiveness and broaden the applicability of this method, extensive comparative experiments and theoretical calculations were conducted to reveal its underlying synthetic mechanisms.

The iodine plays an irreplaceable role in the STT synthesis of crystalline RP. Despite the high vacuum environment within the quartz ampoule, the sublimation of aRP at low temperatures (<500 °C) remains minimal. This is due to the disordered polymer chain structure of aRP, which requires considerable atomic bond rearrangement for

the transformation from RP to P_4. Consequently, this transformation is kinetically hindered, limiting aRP sublimation at low temperatures and affecting the subsequent synthesis of crystalline RP. We found that the addition of iodine can significantly improve this process. While iodine is traditionally employed as a transport agent in CVT reactions, it assumes a predominant catalytic role for RP sublimation in the P/I_2 system[32]. Iodine possesses a dramatically low sublimation temperature (~45 °C). The sublimated iodine molecules can embed in aRP and disrupt its chain-like bonding system, thereby accelerating the kinetic processes and facilitating the catalytic sublimation of RP at low temperatures.

After identifying the role of iodine, a GPM solid-solid phase transition model was proposed to describe the STT synthesis of crystalline RP powders at hot end, which can be categorized into three main processes: i) iodine molecule embedding, ii) aRP sublimation, and iii) P_4 molecule-mediated in-situ reconstruction of solid RP. Specifically, sublimated iodine molecules embed in aRP, catalyzing the sublimation of aRP to generate P_4 molecules. These mobile P_4 molecules then participate in the in-situ reconstruction to form crystalline RP powders via inverse reactions (Fig. 3a).

The entire GPM solid-solid phase transition process continues throughout the reaction time span, with solid RP and gaseous P_4 molecules maintained in a state of dynamic equilibrium. Upon entering the isothermal stage, the partial pressure of P_4 approaches its saturation vapor pressure at the reaction temperature (465–450 °C), estimated to be approximately 1.760 bar to 2.666 bar (Supplementary Fig. 13). This relatively high P_4 vapor pressure facilitates the continuous transformation of aRP into crystalline RP. In contrast to the iodine-containing system, in a pure phosphorus system, the sublimation of RP is significantly limited by kinetic constraints, resulting in a slow sublimation rate. Consequently, the system remains in a non-equilibrium state throughout the reaction duration, with the P_4 vapor pressure far below its saturation value. Under such conditions, the relatively low P_4 vapor pressure hinders the transformation of aRP, and within the same reaction time, only a small amount of conversion occurs on the surface of aRP (Supplementary Figs. 14–16). Moreover, the physical state of the RP precursor plays a critical role in regulating the gas pressure in the reaction system as well. Under the same reaction conditions, aRP in powder form undergoes complete transformation into fibrous Form IV RP, whereas bulk aRP largely retains its original non-crystalline block structure (Supplementary Figs. 17, 18). This is because the ground powder possesses a higher specific surface area, which enables more effective interaction with iodine and P_4 molecules during the reaction. As a result, aRP can sublimate more rapidly to reach saturated vapor pressure and facilitate faster in-situ transformation. In contrast, bulk aRP, with its significantly lower surface area, exhibits much slower sublimation due to insufficient contact with reactants, leading to a prolonged low vapor pressure environment. Furthermore, limited contact between P_4 molecules and bulk aRP also slows the in-situ conversion into crystalline RP.

Notably, due to the inherent transport property of iodine, a portion of the sublimed P_4 molecules will inevitably be transported to the cold end of the quartz ampoule, forming a polycrystalline RP coating as a byproduct. Although inverse or isothermal temperature setting can enable the selective synthesis of crystalline RP at the hot end while reducing product loss caused by vapor transport, our results indicate that, in the absence of transport, the phase transformation of RP remains incomplete under the same reaction duration (Supplementary Fig. 19). A significantly longer holding time is required to achieve phase-pure crystalline RP. This discrepancy can be attributed to the dynamic flow of gaseous species between the hot and cold ends under transport conditions, which facilitates more sufficient contact between gas-phase molecules and RP particle surfaces, thereby significantly accelerating the transformation rate. However, the trade-off introduced by the transport effect is also evident: as the reaction proceeds, the crystalline RP product at the hot end is continuously consumed and transported away, resulting in a gradual reduction in overall yield. Thus, obtaining high-purity crystalline RP requires a balance between reaction time and product yield. In this context, it is particularly important to retain the beneficial effects of transport while appropriately reducing its transport rate. Theoretically, the transport rate (J) in a CVT reaction system can be described by Schäfer's transport equation[33]:

$$J \propto \frac{P_i}{\sum P_i} \cdot \frac{s}{l} \cdot \bar{T}^{0.75} \tag{1}$$

where s and l are the cross-section are and transport length of the quartz ampule, respectively, $\bar{T}$ is the mean temperature along the transport path, P_i and $\sum P_i$ represent the partial pressure of the effective transport species and the total pressure, respectively.

In our system, the reaction can be conducted at a lower temperature (465 °C) due to the iodine-catalyzed sublimation of aRP precursor. Additionally, the low saturated vapor pressure of RP at reduced temperatures (465 °C) decreases the partial pressure of P_4 molecules by an order of magnitude compared to that at higher temperatures (550 °C), which results in a reduction of $\frac{P_i}{\sum P_i}$ value, further slowing the transport rate while enhancing safety (Supplementary Fig. 20). Furthermore, setup modifications such as the introduction of neck and sand cores within the quartz ampoule also contribute to decreased transport rate (Supplementary Figs. 21,22). Combining the above strategies, our low-temperature CVT reaction system exhibits a significantly reduced P_4 molecules transport rate compared with conventional CVT systems (Fig. 3b, c and Supplementary Fig. 23). Therefore, while preserving the transport effect, we significantly suppressed deposition at the cold end and enhanced reconstruction and transformation at the hot end.

To further investigate the time-dependent phase-selective synthesis of crystalline RP, STT reactions with holding times ranging from 0 to 30 hours were conducted. As the holding time increased, the color of the RP powders gradually transitioned from dark to light (Fig. 3d and Supplementary Fig. 24). In addition to the specific holding time of the synthesized single phase, RP powders at intermediate stages exhibited distinct mixed colors, indicating a transition state in which two crystal phases coexisted (Supplementary Fig. 25). It was further confirmed by PXRD and SEM (Fig. 3e and supplementary Figs. 26–41). The precursor aRP exhibits a characteristic broad peak near 15°, indicative of its amorphous state. When the holding time was 0 hours, a portion of the bulk aRP was converted to Form II nanostructured rods, with the broad peak of aRP at 15° shifting to a sharper diffraction peak characteristic of Form II. After extending the holding time to 0.5 h, all the aRP was converted to Form II, and the diffraction peak near 15° narrowed and sharpened, indicating a reduction in the amorphous phase. As the holding time continued to increase, characteristic diffraction peaks of Form IV emerged, with intensity gradually increasing. At holding time of 1 hours and 2 hours, the crystalline RP existed as a mixture of Form II and Form IV. When the holding time reached 3 hours, Form II was completely converted to Form IV. As the holding time continued to extend, a diffraction peak at 16.4°, corresponding to the (004) plane of Form V, appeared, and with the intensification of the Form V peak, the Form IV diffraction peak gradually weakened. Unlike the evolution from Form II to Form IV, within a wide range of holding time, the crystalline RP remained in a two-phase coexistence state of Form IV and Form V. It is important to note that when the holding time was extended to 30 hours, Form IV was almost entirely converted to Form V, although a small impurity phase of less than 1% (Form IV) still remained. This is a common occurrence in the synthesis of Form V, and we will discuss the reason in a later section. Furthermore, UV-vis-

https://doi.org/10.1038/s41467-025-63668-9

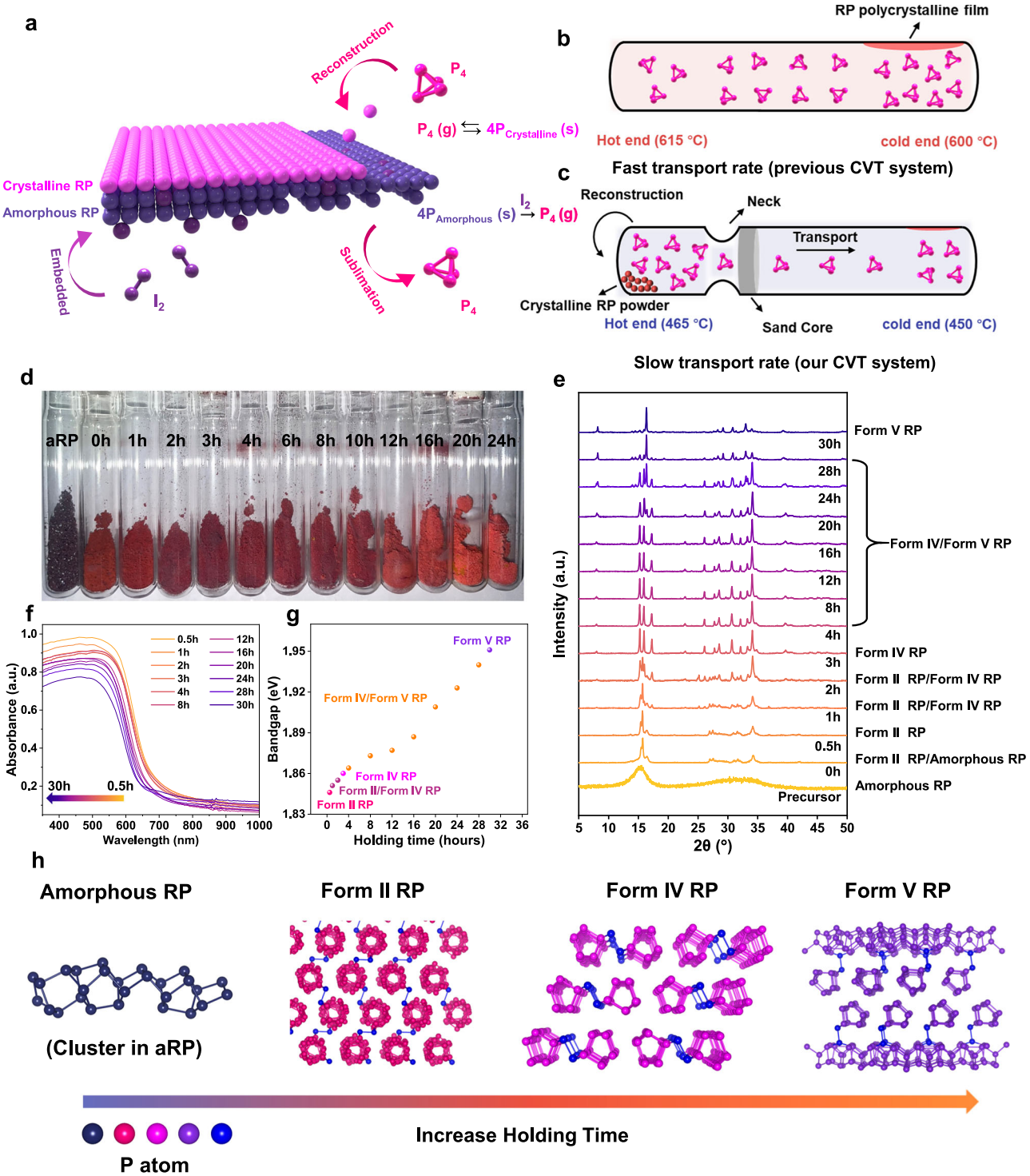

Fig. 3 | Synthetic mechanisms of the STT method. a Schematic diagram of the gas-phase molecule-mediated (GPM) solid-solid phase transition model. **b, c** Schematic illustration of the conventional CVT method and our system for transport rate control, respectively. **d** Photographs of quartz ampoules containing crystalline RP powders after the STT reactions with 0 to 24 hours holding time. **e** PXRD pattern of the crystalline RP powders obtained after the STT reaction with holding time ranging from 0 to 30 h. **f** UV-vis-NIR absorption spectra of crystalline RP powders with different holding time in (**e**), and (**g**) corresponding extracted optical bandgap distribution maps. **h** Schematic diagram of the continuous evolution of amorphous-Form II-Form IV-Form V with prolonged holding time.

NIR absorption spectra show that as the holding time increased, the gradual transformation of crystalline RP caused a gradual blue shift of the absorption edge, and the optical bandgap steadily increased, which was consistent with the color change of the samples (Fig. 3f, g, and Supplementary Fig. 42). These results indicate that the time-dependent phase-selective synthesis of crystalline RP does not occur via a direct conversion of the aRP precursor, but instead proceeds through a sequential phase evolution: amorphous-Form II-Form IV-Form V. The entire phase evolution of crystalline RP follows the GPM solid-phase transformation mechanism, yet each stage involves distinct precursor states. Accordingly, we further extended the GPM mechanism by refining the aRP (Form I)-crystalline RP transformation into three specific transitions: Form I → Form II, Form II → Form IV, and Form IV → Form V, as shown in Supplementary Figs. 43–45.

Structural evolution of crystalline RP in GPM solid-solid phase transition

The experimental results above demonstrate that the continuous evolution of RP exists during the GPM solid-solid phase transition process. Therefore, the specific crystalline RP can be efficiently synthesized by regulating the holding time. This raises two significant and intriguing questions: why does crystalline RP follow the transformation sequence of Form II-Form IV-Form V, and what specific structural evolution occurs throughout this process? Therefore, a more detailed investigation into the continuous evolution of crystalline RP is urgently demanded for a deeper understanding of the polymorphic transformation.

Through density functional theory (DFT) calculations, it was found that the electronic energy of aRP lies between that of white phosphorus (WP) and crystalline RP (Fig. 4a and Supplementary Tables 3, 4). Among several crystalline RP, the electronic energy of Form II, IV, and V decreases sequentially. It indicates that the phase transition of amorphous-Form II-Form IV-Form V is thermodynamically favorable, gradually progressing toward the most stable crystalline phase with the lowest energy, consistent with previous reports[34]. To further investigate the phase transition of crystalline RP from a kinetic perspective, the process was divided into two stages: Form II-Form IV (0–3 hours) and Form IV-Form V (3–30 hours). Figure 4b, c show the time-dependent relative content curves at a given temperature, exhibiting the characteristic S-shaped profiles of solid-solid phase transition. For Form II-Form IV transition, the half conversion time is only 113 min, while for Form IV-Form V transition, it takes up to 1011 min. It indicates that kinetically, the conversion rate of Form II-Form IV is fast, allowing Form II to quickly convert into Form IV. In contrast, the transformation from Form IV to Form V is significantly slower, resulting in the coexistence of Forms IV and V over a broad range of holding time.

Furthermore, the possible structural evolution process during the GPM solid-solid phase transition from Form II to Form IV was explored. It is worth noting that Form II features a phosphorus tube structure, similar to that of Form IV, which consists of multiple P8 and P9 building blocks connected via P2 and extending infinitely along the *w*-axis (Fig. 4d). Based on the previously mentioned sublimation-reconstruction equilibrium, it inspires us that the mobile P_4 molecules sublimated from Form II in the gas phase may take this phosphorus tube structure as a growth template. New structural units would be continuously added at the end of the tube along the *w*-axis, thereby reconstructing the parallel double-tube configuration of Form IV and facilitating the transformation from Form II to Form IV. Therefore, based on the structural subunit of Form II, a series of potential intermediates (Int) featuring parallel double-tube motifs along the *w*-axis were constructed, and CP2K was employed to calculate the energy of these stable configurations (Supplementary Fig. 47). The starting Form II structural subunit is the most unstable among several configurations, possessing the highest electronic energy (Fig. 4e and Supplementary Table 5). While the construction of the parallel double-tube motif at the end of the Form II subunit was found to be energetically favorable, with the electronic energy of intermediates Int-1 to Int-5 lying between those of the Form II subunit and Form IV, and the energy of the system decreased progressively with the gradual completion of the terminal parallel double-tube structure. The similar growth behavior was observed in certain regions of the polycrystalline film at the cold end, where Form IV grew sequently along the terminal end of pre-existing Form II (Supplementary Fig. 48a). When the amount of aRP precursor was reduced by half, the initial growth of one-dimensional small grains of Form IV became more obvious at the terminal end of Form II (Supplementary Fig. 48b). The crystal phases on the surface were distinguished through Raman mapping (Supplementary Fig. 49). Additionally, the Form II-Form IV intermediate with one-dimensional morphology were further obtained through liquid-phase exfoliation (Supplementary Fig. 50a). Although no distinct boundary is apparent between Form II and Form IV in the one-dimensional rod growth direction in the image, Raman line scanning reveals a transition from Form II to Form IV as the measurement points moved downward (Supplementary Fig. 50b and Fig. 4f). The corresponding Raman contour plot more clearly illustrates the transition from Form II to Form IV and defines the boundary (Fig. 4g). Overall, the transformation of Form II-Form IV is a process of increasing structural order. The sublimated P_4 molecules continue to grow at end of the higher-energy, metastable solid Form II RP and subsequently transform to stable solid Form IV with lower energy (Fig. 4h).

Nevertheless, the structural evolution in the GPM Form IV-Form V solid-solid phase transition is considerably more complicated. Different from the one-dimensional structure in Form II and Form IV, where adjacent pentagonal phosphorus tubes are arranged parallel to each other, the perpendicular arrangement of these tubes in Form V results in a two-dimensional layered structure, which hinders its continuous growth along the end of Form IV phosphorus tubes like the transformation from Form II to Form IV. Meanwhile, if the phosphorus tubes of Form IV are completely opened and recombined through mobile P_4 molecules to grow into Form V, a massive structural rearrangement would be required. Considering that the only structural difference between Form IV and Form V lies in the arrangement of the phosphorus tubes, it suggests that Form IV may first transition through an intermediate stage involving a single phosphorus tube dissociating from Form IV during the transformation process, which then assembles to obtain Form V through growth (Fig. 5a). To verify the feasibility of dissociation-assembly mechanism, integrated crystal orbital Hamilton population (ICOHP) was employed to analyze the impact of differences in phosphorus tubes arrangement on chemical bonding within the structure, especially the bridging bond connecting the twin tubes (Fig. 5b, c). As shown in Fig. 5d, the P-P bond lengths in the Form IV and Form V range from 2.18 Å to 2.31 Å, with all P-P bonds having -ICOHP values greater than 0, indicating that bonding interactions are dominant. It is noteworthy that the bridging bond in the Form V structure not only has the shortest bond length (2.18 Å) among all P-P bonds, but also exhibits a significantly high -ICOHP value (5.23), indicating a strong bonding interaction between the twin tubes. In contrast, the -ICOHP value of the bridging bond in the Form IV structure (4.64) is considerably lower, which suggests a much weaker bonding interaction, thereby facilitating the dissociation of Form IV into a single tube intermediate. This difference arises from the twisted structure of Form V, which lowers the energy of the lone pair electrons on the bridging phosphorus atoms[13]. Consequently, during the conversion from Form IV to Form V, both structures undergo a dissociation-assembly equilibrium, and the difference in bonding strength of the bridging P-P bond drives the continuous transformation from Form IV to Form V (Fig. 5a).

Additionally, we further investigated the possibility of obtaining Form V through a dissociation-growth mechanism based on the single phosphorus tube intermediate. Unlike the structural changes observed in the one-dimensional direction during the conversion from Form II to Form IV, it is challenging to consider multi-directional structural changes in a periodic system unless vacuum layers are added along these directions to isolate the system, which would significantly increase the computational cost. To simplify the calculations, we selected structural subunits from the unit cells of Form IV and Form V as molecular fragments and demonstrated the possible evolutionary pathway through the extension growth of phosphorus cluster molecules (Fig. 5e). Specifically, the parallel twin tubes structure of the Form IV subunit, which contains 42 atoms, dissociates during the conversion process to form a single tube intermediate structure containing 21 atoms. To stabilize the P21 intermediate and reduce the energy of the non-bonding lone pairs of the bridging phosphorus atoms, a P9 phosphorus cluster, formed from P_4 molecules in the high-temperature gas phase, combines with the P21 intermediate by

https://doi.org/10.1038/s41467-025-63668-9

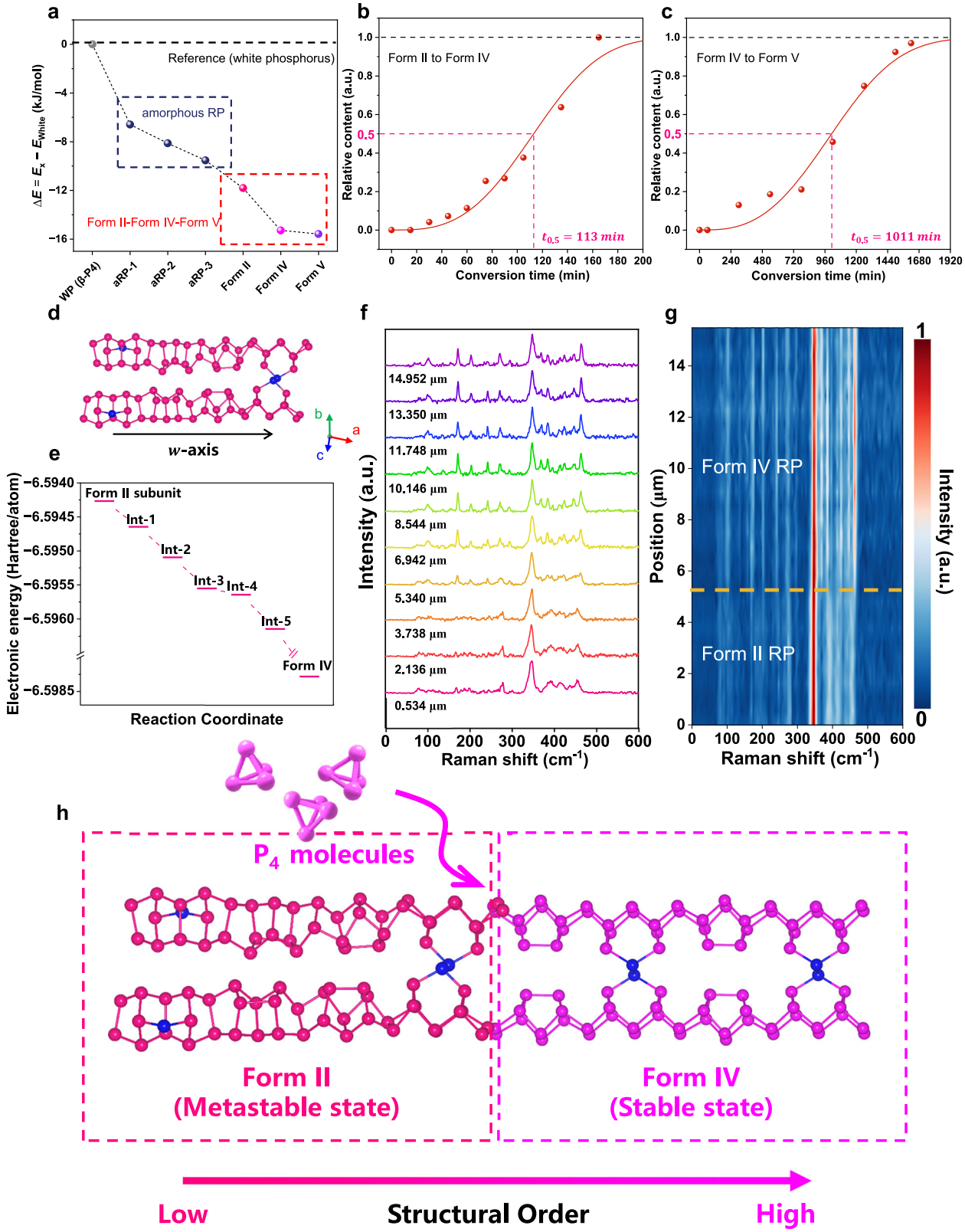

Fig. 4 | Structural evolution in the GPM Form II-Form IV solid-solid phase transition. a Electronic energy distribution diagram of different elemental RP calculated theoretically, with β-white phosphorus (WP) as the energy reference. The structural order degree of the three aRP phases (1, 2, and 3) increases sequentially[42]. **b**, **c** The curve of relative content of Form IV (Form II-Form IV transition) and Form V (Form IV-Form V transition) as a function of conversion time, respectively. Note: See Supplementary Information for details on the calculation of relative contents. **d** Crystal structure of Form II, with the horizontal direction representing the *w*-axis ($w = 2a + b$). **e** Calculated electronic energy distribution diagrams of Form II subunits, Form IV, and the intermediates in the Form II-Form IV transition. **f** The Raman spectrum variation with the position of the scanning point obtained by line scanning along the one-dimensional rod growth direction and **g** the corresponding Raman contour plot. The orange dashed line indicates the boundary between Form II and Form IV. **h** Schematic diagram of the transformation of Form II-Form IV. Note: Data used in (**a**, **e**) are summarized in Supplementary Table 2 and Table 3, respectively.

https://doi.org/10.1038/s41467-025-63668-9

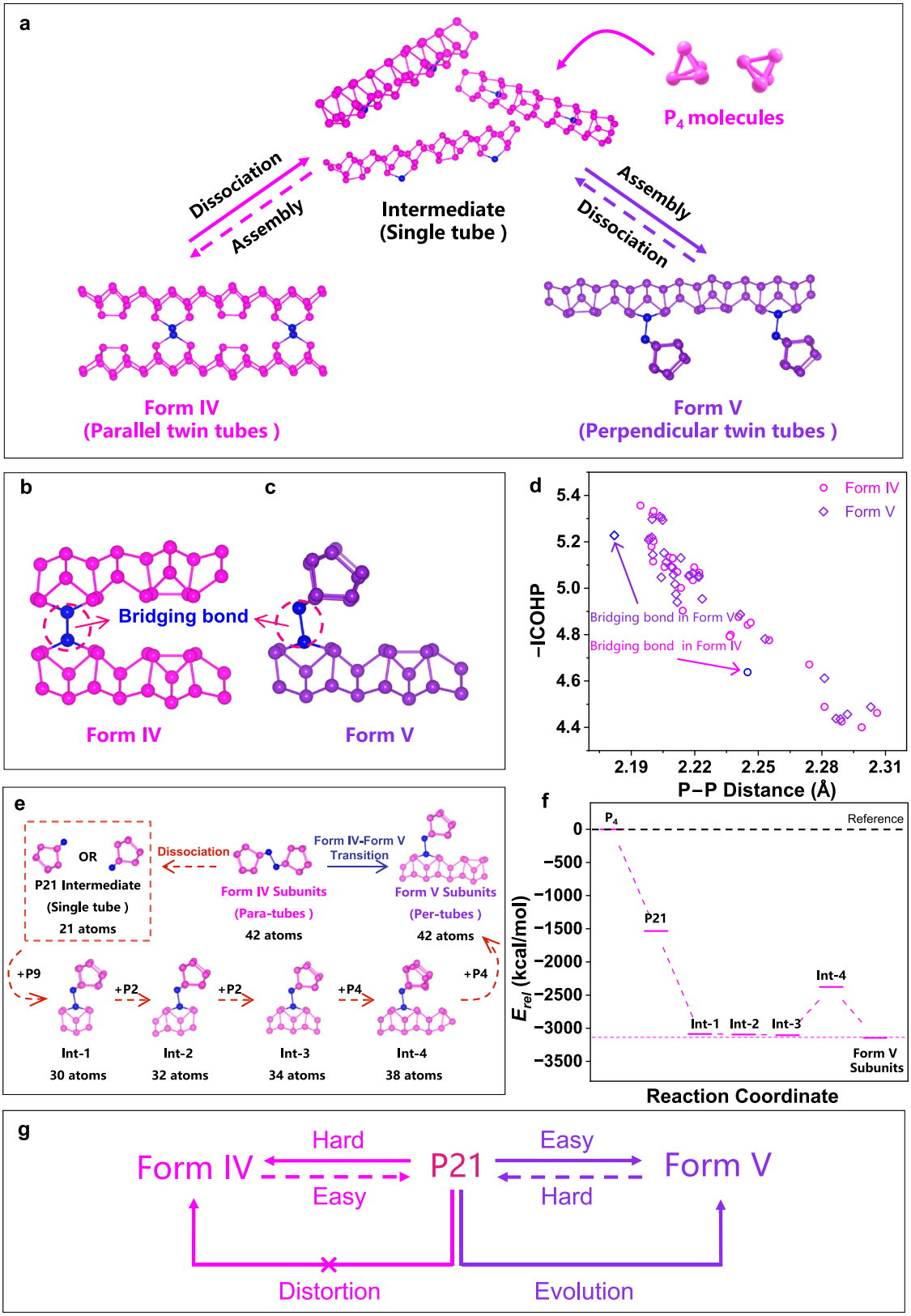

Fig. 5 | Structural evolution in the GPM Form IV-Form V solid-solid phase transition. a Schematic diagram of the transition from Form IV to Form V via a single tube intermediate. **b, c** Structural subunits of Form IV and Form V, respectively. The red dashed circles indicate the bridging P-P bond connecting twin tubes. **d** The distribution diagram of integrated crystal orbital Hamilton population (-ICOHP) values and bond lengths for all P-P bonds in Form IV and Form V. **e** Schematic diagram of the structural evolution of Form V subunits formed by extension growth based on the single tube P21 intermediate. **f** Calculated relative electronic energy distribution diagrams of intermediates in the Form IV-Form V transition. **g** Summary diagram of the conversion pathway based on the P21 intermediate.

twisting angle to form the perpendicular twin tubes configuration, Int-1. Subsequently, based on Int-1, the structure grows progressively along the P9 cluster tube direction to yield intermediate structures Int-2, Int-3, and Int-4, ultimately growing into the perpendicular twin tubes structure of Form V subunits, which also contains 42 atoms. The structural optimization and energy calculations of these intermediate structures were performed using Gaussian (Supplementary Figs. 51, 52 and Supplementary Table 6). Figure 5f shows the variation of energy with reaction progress during the evolution of molecular structure, using P_4 molecule as the energy reference. Due to the presence of unsaturated bridging phosphorus atoms, the single tube P21 intermediate has the highest energy and is the most unstable; when the P9 cluster combines with it to form Int-1, the single tube structure becomes stabilized, and the energy is significantly reduced. During the subsequent growth along the phosphorus chain direction defined by the P9 cluster, the addition of P2 linking units on both sides of the cluster has little impact on the overall structural energy, with the energies of Int-2 and Int-3 exhibiting only slight decreases. However, the addition of a high-energy P_4 molecule onto the P2 link results in the formation of an unstable, distorted P4 unit at the chain edge, causing a significant increase in the energy of Int-4. When this distorted P_4 unit further combines with another P_4 molecule to form a more stable P8 cluster, the structure becomes considerably more stable, leading to a sharp energy decrease. It should be noted that, unlike the intermediates in the Form II–Form IV transformation, in which the significantly decreasing energies were calculated under periodic boundary conditions, the results only represent the energy evolution trend within a single growth unit (from Int-1 to the Form V subunits). As the growth continues, the overall system energy is expected to further decrease progressively. Alternative growth pathways further confirm the consistency of the energy variation trend among intermediate structures (Supplementary Figs. 53, 54 and Supplementary Table 7). Furthermore, we carried out thermodynamic energy corrections for the intermediate structures at 20 atm under different temperatures (Supplementary Fig. 55). Supplementary Tables 8–10 summarize the electronic energy (E_{ele}), zero-point energy corrected energy, internal energy (U), enthalpy (H), and Gibbs free energy (G) of the intermediate structures at 538 K, 638 K, and 738 K, respectively. Compared to the electronic energies, the internal energies of the intermediates decrease with increasing temperature, indicating enhanced structural stability at elevated temperatures. More importantly, the energy differences observed along the transformation from Int-1 to the Form V subunits become increasingly significant at higher temperatures, with a more pronounced downward trend in energy (Supplementary Fig. 56, 57 and Supplementary Table 11). This suggests that higher temperatures are more favorable for this growth mode.

Besides, the potential growth pathway for the evolution of the single tube P21 intermediate to the parallel twin tubes structure of Form IV subunits was also explored (Supplementary Fig. 58). Nevertheless, after structural optimization, all initial structures underwent the distortion without exception (Supplementary Fig. 59). To lower the energy of the lone electron pairs in the bridging bonds, the optimized parallel twin tubes structure rotates by a certain angle, approaching the perpendicular twin tubes configuration. It further demonstrates that in the stepwise growth mode with P21 as the intermediate, the system tends to transition towards the perpendicular twin tubes structure of Form V. This distinction also facilitates the continuous transformation from Form IV to Form V. Notably, the more complicated structural evolution of Form IV-Form V, compared to that in Form II-Form IV, accounts for the difference observed during the dynamic process.

In summary, due to the differences in bonding strength, Form IV is more easily dissociated to obtain the P21 intermediate by breaking the bridging P-P bonds compared to Form V (Fig. 5g). The resulting P21 intermediate will then self-assemble through bonding to regenerate either Form IV or Form V, with the latter being easier to obtain due to its stability and stronger valence bonding. Meanwhile, the P21 intermediates can also transform into Form V through gradual evolution, while structural distortions in the intermediates block the evolution from P21 to Form IV. Hence, whether through dissociation-assembly or dissociation-growth, these two growth modes, based on the single tube P21 intermediate, collectively facilitate the conversion of Form IV to Form V. Yet simultaneously, the presence of equilibrium renders the conversion incomplete, resulting in a small amount of Form IV persisting during the synthesis of Form V.

Basic framework in the polymorphic transformation of crystalline RP

After elucidating the transformation correlation and structural evolution of crystalline RP, another important question arises: previous studies have predominantly relied on temperature control to synthesize crystalline RP of different phases, whereas we achieved this through time control (Supplementary Fig. 60). Could there be a unified framework that integrates both approaches and guides the controlled synthesis and polymorphic transformation of crystalline RP?

The stepwise phase transition behavior of crystalline RP aligns with the empirical description of intermediate stages during phase transitions proposed by Ostwald in 1897, known as the rule of stages[35,36]. Ostwald's rule of stages states that during a phase transition, an unstable system does not directly reach the most stable phase. Instead, it progresses through a series of metastable intermediate phases, each of which is more stable than the preceding one. While these metastable phases are thermodynamically suboptimal, they are kinetically easier to form. Building on this understanding and supported by our experimental observations, we have extended Ostwald's rule to describe the polymorphic transformation of crystalline RP. In accordance with this rule, the energy barrier ΔG^*_{I-II} associated with the transition from initial Form I (i.e., aRP) to Form II is expected to be the lowest among the energy barrier for subsequent transitions, following the sequence of $\Delta G^*_{I-II} < \Delta G^*_{II-IV} < \Delta G^*_{IV-V}$.

Hence, a comprehensive framework encompassing both temperature and time control for the polymorphic transformation of crystalline RP is proposed, as demonstrated in Fig. 6. For temperature control, at a given holding time, when the reaction temperature is low, the thermal fluctuations in the system can merely overcome the lowest energy barrier, ΔG^*_{I-II}, resulting in Form II. As the temperature increases, the system energy can cross higher barriers, ΔG^*_{II-IV}, but due to the increased reaction rate and constant reaction time, this stage-wise phase transition is not readily observed. As a result, the process macroscopically manifests as a direct transition from Form I to Form

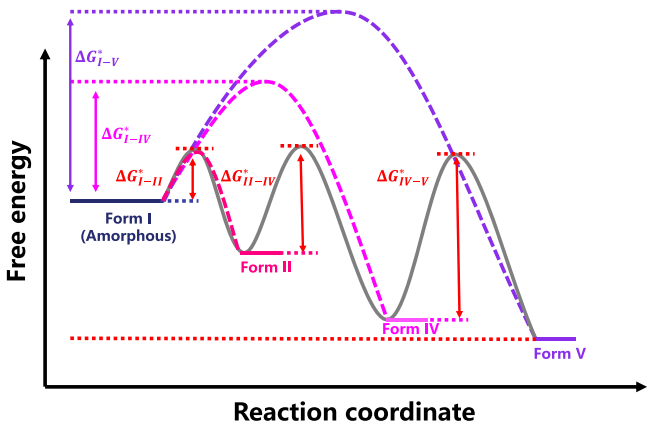

Fig. 6 | Schematic diagram illustrating the basic framework in the polymorphic transformation of crystalline RP. Each ΔG^* represents a qualitative estimate of the relative energy barrier that must be overcome during the transformation process, as inferred from Ostwald's rule of stages.

IV, crossing the barrier, ΔG^*_{I-IV}. As the temperature continues to rise, the system energy can directly surpass the highest barrier, ΔG^*_{I-V}, achieving a direct transition from Form I to Form V.

In the case of time control, the reaction temperature remains constant, meaning the system can only overcome energy barriers through sustained thermal fluctuations. The initial transformation resembles the low-temperature stage of temperature control, where Form I first surmounts the lowest energy barrier to obtain the metastable Form II. A distinct kinetic feature then emerges: as time progresses, metastable Form II gradually passes through the subsequent energy barrier, ΔG^*_{II-IV}, and fully transforms into Form IV. Subsequently, Form IV continues this process, gradually surpassing the highest barrier, ΔG^*_{IV-V}, and slowly transforms into the more stable Form V.

This irreversible, stagewise phase transition behavior is further confirmed experimentally. Unlike the previous method, which only used Form I as the starting material and varied the holding time, we additionally selected Form II and Form IV as independent starting materials to assess the phase transition possibilities at each stage by extending the holding time (Supplementary Figs. 61–64). Specifically, in the first stage, Form I was used as the starting material, and after 0.5 hours of heating, the expected Form II was obtained. In the second stage, the previously obtained Form II was used as the precursor, and after an additional 3.5 hours of heating, the more stable Form IV was successfully obtained. In the third stage, Form IV obtained in the second stage was heated for another 28 hours, yielding the most stable Form V as well. Additionally, we conducted phase transition experiments using plate-like Form II RP, synthesized via a solvothermal method, as the phosphorus precursor. After a holding time of 4 h, the product at the hot end remained as Form II RP; however, its morphology began to transform from the original 2D platelets into 1D nanorods (Supplementary Fig. 65a–d). With extended holding times of 8 h and 12 h, the formation of Form IV and subsequently Form V RP was progressively observed in the products (Supplementary Fig. 65e–h).

Above results not only strongly confirm the independent stagewise phase transitions within the basic framework but also further demonstrate the continuity of the crystalline RP transformation. In conclusion, regardless of the crystal phase of RP precursor or the extent of the reaction, the basic framework can theoretically guide the controlled conversion of crystalline RP to the next phase.

Discussion

In summary, we achieved the selective synthesis of the Form II, IV, and V crystalline RP powders via a STT method based on a low-temperature CVT reaction system. The morphologies, structures, and spectral characteristics of the three highly crystalline RP were analyzed using SEM, HRTEM, PXRD, UV-vis-NIR absorption, PL and Raman spectra. The GPM solid-solid phase transition model was proposed to describe the transformation process, encompassing iodine molecule embedding, aRP sublimation, and P_4 molecule in-situ reconstruction. The synthetic mechanism of the STT method was investigated in depth, which can be attributed to two key factors. First, based on the GPM solid-solid phase transition mechanism, the iodine-catalyzed sublimation of aRP facilitates the STT reaction at low temperature, reducing the vapor transport rate and promoting in-situ reconstruction and phase transformation. Second, the continuous evolution of crystalline RP allows for selective synthesis with controlled holding time. The combination of these two effects achieves the low-temperature phase-selective synthesis of crystalline RP. Additionally, the continuous evolution of crystalline RP was thoroughly investigated through theoretical calculations and experiments. The phase transition of crystalline RP follows a thermodynamically favorable sequence: Form II-Form IV-Form V, each exhibiting distinct kinetic characteristics. Specifically, the half conversion time from Form II to Form IV is 113 min, while the half conversion time from Form IV to Form V is 1011 min. Furthermore, we have elucidated the structural evolution from Form II to Form IV, where P_4 molecules continue to grow at the metastable end of Form II, gradually forming a more stable parallel double structure, ultimately transitioning towards the lower-energy Form IV. In contrast, the structural evolution from Form IV to Form V is driven by the varying strength of the bridging P-P bonds, which facilitates bond cleavage in Form IV, leading to the formation of a single tube P21 intermediate. This intermediate then reassembles or grows, resulting in the more stable Form V. Based on the Ostwald's rule, we have established a unified framework that integrates both temperature-controlled and time-controlled methods, providing a comprehensive reference for the controllable synthesis and polymorphic transformation of crystalline RP. Our work has facilitated the phase-selective synthesis of crystalline RP, provided a deeper understanding of the transition process of phosphorus, and laid a solid theoretical foundation for the synthesis and polymorphic transformation of non-metal elements.

Methods

Materials synthesis

Synthesis of three high-quality crystalline RP powders. Form II, Form IV, and Form V crystalline RP powders were synthesized through a STT method based on a low-temperature CVT reaction system. Typically, aRP powders (Alfa Aesar, 99.999%, ~400 mg) and iodine particles (Alfa Aesar, 99.9%, ~18 mg) were mixed and loaded into a 14 cm quartz ampoule with an inner diameter of 8 mm. Additionally, a neck with an inner diameter of 4 mm and a sand core with a G4 pore size and 7.7 mm inner diameter were introduced to control the transport. Subsequently, the quartz ampoule was evacuated to 1.0×10^{-3} Pa and sealed by vacuum sealing (MRVS-1002, Partulab). The sealed ampoule was then placed horizontally in a two-zone tube furnace (OTF-1200X-II, Kejing), with the precursor positioned at the hot end. The ampoule was then heated according to a predetermined temperature program. Specifically, the furnace was heated to 465 °C at hot end (450 °C at cold end) at a heating rate of 5 °C/min, maintained for various holding time, and then allowed to cool to room temperature at a rate of 2 °C/min. It is important to note that the same synthesis process was employed in the subsequent discussions, with only adjustments made to the reaction materials and holding time when investigating the corresponding synthetic mechanisms.

Synthesis of polycrystalline RP coating. To compare the effect of temperature on the gas phase transport, the same synthesis process as described above was used in the conventional CVT method, with the only modification being the adjustment of the maximum temperature. The specific temperature program is as follows: the furnace was heated to 615 °C at hot end (600 °C at cold end) at a heating rate of 5 °C/min, maintained for 3 h, and then allowed to cool to room temperature at a rate of 2 °C/min.

Sample preparation for TEM analysis

In a standard liquid exfoliation experiment, crystalline RP powders were first added to a 5 mL isopropanol (IPA) solution in a glass bottle. To minimize oxidation, the bottle was flushed with argon gas and sealed tightly with parafilm. The mixture was then subjected to ultrasonication in a bath at 100 W (KQ2200DB, Kunshan Ultrasonic Instruments) for 60 min. Following the exfoliation process, the suspension was centrifuged at 3000 rpm for 5 minutes to eliminate any residual particles. A small volume of the supernatant was carefully collected and placed onto a copper grid for TEM analysis.

Sample characterizations

Optical microscope (OM), scanning electron microscope (SEM) and high-resolution transmission electron microscope (HRTEM). The

optical micrographs were obtained using a microscope equipped with a 50× magnification objective (BX 51 M, Olympus). The morphology images were captured by SEM (SU8010, Hitachi) at 15 kV. The high-angle annular dark field-scanning transmission electron microscopy (HAADF-STEM) images and elemental mappings were recorded at low-magnification using a TEM equipped with an energy dispersive X-ray spectroscope (EDX). The lattice fringe images and selected area electron diffraction patterns were obtained using a high-resolution TEM (JEM 2100 F, JEOL) at 200 kV.

Powder X-ray diffraction (PXRD) and X-ray photoelectron spectroscopy (XPS). The PXRD patterns were collected using a Bruker D8 Advance diffractometer with Cu-Kα radiation (λ = 1.5406 Å) at 40 kV and 40 mA. The valences of P, C, and O elements were determined using X-ray photoelectron spectroscopy (PHI Quantro SXM, ULVAC-PHI) with monochromatic Al Kα (hν = 1486.7 eV) as the excitation source.

Photoluminescence (PL) and Raman spectra. PL and Raman spectra were collected by a multifunctional spectral imaging microscope (WITec Alpha300RAS, Oxford) equipped with a 50× magnification objective using 532 nm laser excitation at room temperature. For the PL single spectrum test, collection time was 5 seconds with 2 accumulations at a laser power of about 500 μW. For the Raman single spectrum test, collection time was 15 seconds with 1 accumulation at a laser power of about 500 μW. The Raman line scanning and Raman mapping were both taken with a step size of 0.5 μm.

Ultraviolet-visible-near infrared (UV-vis-NIR) absorption spectrum. The UV-vis-NIR absorption spectrum was measured using a spectrophotometer (L950, PerkinElmer) equipped with an integrating sphere in diffuse reflection mode, with $BaSO_4$ as the reference.

Theoretical calculations

Gas phase species calculation. The composition of gas phase species was evaluated using the TRAnsport-Gleichgewichten durch MINimierung der freien Enthalpie (TRAGMIN) 5.1 code[37]. Thermodynamic data were applied as default settings if possible, or sourced from *Thermochemical Data of Elements and Compounds*[38]. A total of five gas phase species (P_4, P_2, I_2, PI_3, Ar) and two solid phases (P(s), I_2(s)), derived from our experiments were included as input variables. Although an inert gas is required for computational purposes, it is not strictly necessary under actual experimental conditions. In this case, 10 mmol of Argon was chosen as the inert gas, while the amounts of RP and iodine were set equivalent to 400 mg and 20 mg to simulate experimental conditions. A simplified one-room model was created for thermal reaction simulations, with the vessel volume fixed at 7.4 mL and temperature series as from 273 K to 923 K.

Electronic energy calculation of phosphorus allotropes. The Vienna ab initio simulation package (VASP) was employed for conducting first-principles calculations[39,40]. The exchange-correlation potential was treated with the generalized gradient approximation (GGA) of the Perdew-Burke-Ernzerhof (PBE) standard functional[41]. The projector augmented wave (PAW) method was used with a plane-wave cutoff energy of 520 eV. The DFT-D3 method was employed to account for van der Waals interactions[41]. Structural optimization started with the refined crystal structure, during which both lattice constants and atomic positions are completely relaxed. It should be noted that the structure of aRP is based on the models derived from theoretical calculations of three ordered structures, with increasing degrees of order, as reported previously[42]. As for Form II, since no experimental crystal structure is available, we have adopted the t41 configuration mentioned in our previous work[15]. Convergence criteria for total energy and atomic forces were set to 10^{-5} eV and 0.01 eV $Å^{-1}$, respectively. The gamma-centered k-point meshes selected for the calculations and optimized lattice parameters of different phosphorus allotropes are summarized in Supplementary Table 1. The Crystal Orbital Hamilton Population (COHP) calculations for Form IV and Form V are based on the optimized structures, and the LOBSTER package was employed to analyze the COHP[43–45]. All the structure models were visualized using the Visualization for Electronic and Structural Analysis (VESTA) program[46].

Structural evolution calculation of Form II-Form IV. The periodic intermediate structures Int-1 to Int-5 were constructed based on the Form II subunits. To simplify the calculation, we selected the structural fragments from Slice1 to Slice3 along the w-axis direction of the t41 configuration of Form II, representing half of a wavy period, as the subunits of Form II. A sufficiently large vacuum layer of 35 Å was incorporated along the a-axis direction of Form II to prevent unnecessary interactions between periodic replicas. The detailed description of the Form II structure can be found in previous work[14,15]. To calculate periodic systems with such a large number of atoms, first-principles calculations were performed using the CP2K package. In the structural optimization, the gamma-centered k-point meshes were set to 1 × 2 × 2, and the basis set used was TZV2P-MOLOPT-GTH. The remaining parameters were consistent with those in the VASP calculations. The input files for the CP2K calculations were partially generated with the assistance of Multiwfn[47].

Structural evolution calculation of Form IV-Form V. Quantum chemistry calculations for the intermediates of molecular fragments in phosphorus clusters within aperiodic systems were performed using the Gaussian16 software[48]. The molecular structures and input files were generated with the GaussView6 visualization tool. Structural optimizations and frequency calculations were conducted at the PBE/6-31 G* level of theory, while single-point energy calculations were carried out using the higher-precision PBE0/6-311 G* method[49].

Data availability

The data that support the findings of this study are available within the paper, its Supplementary Information and Source Data file. Source data are provided with this paper.

References

1. Lange, S., Schmidt, P. & Nilges, T. Au_3SnP_7@black phosphorus: an easy access to black phosphorus. *Inorg. Chem.* **46**, 4028–4035 (2007).
2. Köpf, M. et al. Access and in situ growth of phosphorene-precursor black phosphorus. *J. Cryst. Growth* **405**, 6–10 (2014).
3. Zhang, Z. et al. Two-step heating synthesis of sub-3 millimeter-sized orthorhombic black phosphorus single crystal by chemical vapor transport reaction method. *Sci. China Mater.* **59**, 122–134 (2016).
4. Chen, C. et al. Growth of single-crystal black phosphorus and its alloy films through sustained feedstock release. *Nat. Mater.* **22**, 717–724 (2023).
5. Pielmeier, M. R. P. & Nilges, T. Formation mechanisms for phosphorene and SnIP. *Angew. Chem. Int. Ed.* **60**, 6816–6823 (2021).
6. Li, L. et al. Black phosphorus field-effect transistors. *Nat. Nanotechnol.* **9**, 372–377 (2014).
7. Yuan, S., Naveh, D., Watanabe, K., Taniguchi, T. & Xia, F. A wavelength-scale black phosphorus spectrometer. *Nat. Photonics* **15**, 601–607 (2021).
8. Biswas, S., Grajower, M. Y., Watanabe, K., Taniguchi, T. & Atwater, H. A. Broadband electro-optic polarization conversion with atomically thin black phosphorus. *Science* **374**, 448–453 (2021).
9. Roth, W. L., DeWitt, T. W. & Smith, A. J. Polymorphism of red phosphorus. *J. Am. Chem. Soc.* **69**, 2881–2885 (1947).

10. Krebs, H., Müller, K. H., Pakulla, I. & Zürn, G. Über den Hittorfschen Phosphor und kristallisierte Polyphosphide. *Angew. Chem.* **67**, 524–525 (1955).
11. Thurn, V. H. & Krebs, H. Crystal structure of violet phosphorus. *Angew. Chem.* **5**, 1047–1048 (1966).
12. Thurn, H. & Krebs, H. Über Struktur und Eigenschaften der Halbmetalle. XXII. Die Kristallstruktur des Hittorfschen phosphors. *Acta Crystallogr., Sect. B* **25**, 125–135 (1969).
13. Ruck, M. et al. Fibrous red phosphorus. *Angew. Chem. Int. Ed.* **44**, 7616–7619 (2005).
14. Yoon, J.-Y. et al. Type-II red phosphorus: Wavy packing of twisted pentagonal tubes. *Angew. Chem. Int. Ed.* **62**, e202307102 (2023).
15. Zhang, B. et al. Assessing the structural diversity of Form II red phosphorus via stepwise crystal structure search. *J. Am. Chem. Soc.* **146**, 26369–26378 (2024).
16. Liu, Q. et al. Crystalline red phosphorus nanoribbons: Large-Scale synthesis and electrochemical nitrogen fixation. *Angew. Chem. Int. Ed.* **59**, 14383–14387 (2020).
17. Duan, Z. et al. Large-Scale synthesis of crystalline phosphorus nanosheets with superior air-water stability and flame-retardancy ability. *Chem. Eng. J.* **505**, 159566 (2025).
18. Sun, Z., Zhang, B., Zhao, Y., Khurram, M. & Yan, Q. Synthesis, exfoliation, and transport properties of quasi-1D van der Waals fibrous red phosphorus. *Chem. Mater.* **33**, 6240–6278 (2021).
19. Chen, W. et al. Giant *ab*-plane birefringence in quasi-1D fibrous red phosphorus. *Angew. Chem. Int. Ed.* **63**, e202403531 (2024).
20. Du, L. et al. Giant anisotropic photonics in the 1D van der Waals semiconductor fibrous red phosphorus. *Nat. Commun.* **12**, 4822 (2021).
21. Winchester, R. A. L., Whitby, M. & Shaffer, M. S. P. Synthesis of pure phosphorus nanostructures. *Angew. Chem. Int. Ed.* **48**, 3616–3621 (2009).
22. Eckstein, N., Hohmann, A., Weihrich, R., Nilges, T. & Schmidt, P. Synthesis and phase relations of single-phase fibrous phosphorus. *Z. Anorg. Allg. Chem.* **639**, 2741–2743 (2013).
23. Smith, J. B., Hagaman, D., DiGuiseppi, D., Schweitzer-Stenner, R. & Ji, H.-F. Ultra-Long crystalline red phosphorus nanowires from amorphous red phosphorus thin films. *Angew. Chem. Int. Ed.* **55**, 11829–11833 (2016).
24. Hu, Z., Lu, Y., Liu, M., Zhang, X. & Cai, J. Crystalline red phosphorus for selective photocatalytic reduction of CO_2 into CO. *J. Mater. Chem. A* **9**, 338–348 (2021).
25. Sun, Z. et al. Polarization conversion in bottom-up grown quasi-1D fibrous red phosphorus flakes. *Nat. Commun.* **14**, 4398 (2023).
26. Zhang, S. et al. Synthesis of fibrous phosphorus micropillar arrays with pyro-phototronic effects. *Angew. Chem. Int. Ed.* **62**, e202217127 (2023).
27. Zhang, L. et al. Structure and properties of violet phosphorus and its phosphorene exfoliation. *Angew. Chem. Int. Ed.* **59**, 1074–1080 (2020).
28. Da, Y. et al. Fabrication of single-crystal violet phosphorus flakes for ultrasensitive photodetection. *Small* **20**, 10276 (2024).
29. Binnewies, M., Glaum, R., Schmidt, M. & Schimidt, P. *Chemical Vapor Transport Reactions* (De Gruyter, 2012).
30. Zhang, L. et al. Phonon properties of bulk violet phosphorus single crystals: temperature and pressure evolution. *ACS Appl. Electron. Mater.* **3**, 1043–1049 (2021).
31. Guo, Z., Wu, X., Zhu, T., Zhu, X. & Huang, L. Electron-Phonon scattering in atomically thin 2D perovskites. *ACS Nano* **10**, 9992–9998 (2016).
32. Schäfer, H. & Trenkel, M. Die katalysierte sublimation des roten phosphors. *Z. Anorg. Allg. Chem.* **391**, 11–18 (1972).
33. Binnewies, M., Schmidt, M. & Schmidt, P. Chemical vapor transport reactions-arguments for choosing a suitable transport agent. *Z. Anorg. Allg. Chem.* **643**, 1295–1311 (2017).
34. Bachhuber, F. et al. The extended stability range of phosphorus allotropes. *Angew. Chem. Int. Ed.* **53**, 11629–11633 (2014).
35. Ostwald, W. Studien über die bildung und umwandlung fester körper. *Z. Phys. Chem.* **22U**, 289–330 (1897).
36. Chung, S.-Y., Kim, Y.-M., Kim, J.-G. & Kim, Y.-J. Multiphase transformation and Ostwald's rule of stages during crystallization of a metal phosphate. *Nat. Phys.* **5**, 68–73 (2009).
37. GMIN version 5.1, package TRAGMIN for calculation of thermodynamic equilibrium, www.tragmin.de (accessed: Jan 2025).
38. Binnewies, M. & Milke, E. *Thermochemical Data of Elements and Compounds* (Wiley-VCH, 2002).
39. Kresse, G. & Furthmüller, J. Efficient iterative schemes for ab initio total-energy calculations using a plane-wave basis set. *Phys. Rev. B* **54**, 11169–11186 (1996).
40. Kresse, G. & Joubert, D. From ultrasoft pseudopotentials to the projector augmented-wave method. *Phys. Rev. B* **59**, 1758–1775 (1999).
41. Perdew, J. P., Burke, K. & Ernzerhof, M. Generalized gradient approximation made simple. *Phys. Rev. Lett.* **77**, 3865–3868 (1996).
42. Zhou, Y., Elliott, S. R. & Deringer, V. L. Structure and bonding in amorphous red phosphorus. *Angew. Chem. Int. Ed.* **62**, e202216658 (2023).
43. Dronskowski, R. & Bloechl, P. E. Crystal orbital Hamilton populations (COHP): energy-resolved visualization of chemical bonding in solids based on density-functional calculations. *J. Phys. Chem.* **97**, 8617–8624 (1993).
44. Deringer, V. L., Tchougréeff, A. L. & Dronskowski, R. Crystal orbital Hamilton population (COHP) analysis as projected from plane-wave basis sets. *J. Phys. Chem. A* **115**, 5461–5466 (2011).
45. Maintz, S., Deringer, V. L., Tchougréeff, A. L. & Dronskowski, R. LOBSTER: A tool to extract chemical bonding from plane-wave based DFT. *J. Comput. Chem.* **37**, 1030–1035 (2016).
46. Momma, K. & Izumi, F. VESTA 3 for three-dimensional visualization of crystal, volumetric and morphology data. *J. Appl. Crystallogr.* **44**, 1272–1276 (2011).
47. Lu, T. & Chen, F. Multiwfn: A multifunctional wavefunction analyzer. *J. Comput. Chem.* **33**, 580–592 (2012).
48. Frisch, M. J. et al. *Gaussian 16, Revision C.01*. (Gaussian, Inc., 2016).
49. Francl, M. M. et al. Self-consistent molecular orbital methods. XXIII. A polarization-type basis set for second-row elements. *J. Chem. Phys.* **77**, 3654–3665 (1982).
50. Landi, S. et al. Use and misuse of the Kubelka-Munk function to obtain the band gap energy from diffuse reflectance measurements. *Solid State Commun.* **341**, 114573 (2022).

Acknowledgements

This work is supported by the National Natural Science Foundation of China (No. 52072198 and No. 22571178 for Q.Y.). We acknowledge the Tsinghua Xuetang Talents Program for providing computational resources.

Author contributions

W.C. synthesized and characterized the samples, performed the theoretical calculations, and conducted data analysis. W.C. wrote the original draft. B.Z. gave the guidance on structural modeling and theoretical calculation. Q.L. provided experimental setup and guidance on crystal growth and phase transition. Q.Y. conceived and supervised the project. All authors participated in discussion and editing of the manuscript.

Competing interests

The authors declare no competing interests.

Additional information

Supplementary information The online version contains supplementary material available at https://doi.org/10.1038/s41467-025-63668-9.

Correspondence and requests for materials should be addressed to Qingfeng Yan.

Peer review information *Nature Communications* thanks Jiahong Wang, Yabo Zhu and the other, anonymous, reviewer(s) for their contribution to the peer review of this work. A peer review file is available.